TECHNICAL PAPER

Behavior of concrete-filled steel tubular cold-formed built-up slender square columns under eccentric compression

Rubieyat Bin Ali[1,2] · Md. Mofizul Islam[1,2] · Mahbuba Begum[2] · Md. Soebur Rahman[3]

Abstract

Nowadays, the uses of concrete-filled steel tubular (CFST) columns have been significantly increased in civil engineering infrastructures due to their inherent ductility, high load-bearing capability and excellent energy absorption capacity. This paper presents both experimental and numerical investigations on the structural responses of built-up slender square concrete-filled steel tubular (SCFST) columns under uniaxial eccentric compression. In this study, a total of eleven welded built-up slender SCFST columns were tested with nominal concrete cylinder strengths of 27 MPa, 35 MPa and 44 MPa, respectively. The effects of different parameters including the concrete strength, column overall slenderness ratio, plate slenderness ratio and variation of eccentricities on the buckling modes, ultimate axial strength and post-peak ductility of the specimens were investigated. The test results indicated that the ultimate strength of the columns varied inversely with the load eccentricity ratio. The concrete grades have significant influence on the load-bearing capacity and ductility of the columns. Moreover, the ultimate strength as well as ductility of the tested specimens moderately decreased with the increase of column overall slenderness ratio and plate slenderness ratio, respectively. Thereafter, ABAQUS software was used to develop the finite element (FE) models of the tested specimens. The developed FE models of built-up slender SCFST columns were validated by comparing the simulated results with test results. It was found that the proposed FE models are capable to predict the structural behavior of built-up slender SCFST columns with high accuracy. Finally, the test results were compared with the corresponding failure loads and ultimate bending moments predicted by the EN 1994-1-1 provisions, which appear slightly insecure.

Keywords SCFST column · Built-up steel section · Eccentric compression · Buckling behavior · Finite element model

List of symbols

B	Width of the column
CDP	Concrete damaged plasticity model
DI	Ductility index
E_s	Modulus of elasticity of steel
E_c	Modulus elasticity of concrete
$f_c^/$	Cylinder strength of concrete
f_y	Yield strength of steel
f_u	Ultimate strength of steel
f_r	Residual stress of concrete
F.M	Failure modes
G_F	Fracture energy
G	Global buckling
SY	Steel yielding
W	Welding failure
SD	Standard deviation
T	Wall thickness of the steel tube
L	Length of the column
L/B	Global or column overall slenderness ratio
B/t	Cross-sectional or plate slenderness ratio
e/B	Load eccentricity ratio
$\delta_{m,ut}$	Mid-height lateral deflection at peak load
e	Flow potential eccentricity
ψ	Dilation angle

✉ Rubieyat Bin Ali
rubieyat.bin.ali@gmail.com

Md. Mofizul Islam
mofizul@ugv.edu.bd

Mahbuba Begum
mahbuba@ce.buet.ac.bd

Md. Soebur Rahman
soeburrahman@gmail.com

[1] Department of Civil Engineering, University of Global Village (UGV), Barishal, Bangladesh

[2] Department of Civil Engineering, Bangladesh University of Engineering & Technology (BUET), Dhaka, Bangladesh

[3] Department of Civil Engineering, Military Institute of Science and Technology (MIST), Dhaka, Bangladesh

μ	Viscosity parameter
α_M	Coefficient related to bending of a composite column
k	Amplification factor
β	Equivalent moment factor
M_{ut}	Ultimate bending moment
M_{Ed}	Design bending moment
$M_{pl,N,Rd}$	Design value of the plastic resistance moment of the composite section taking into account the compressive normal force
M_{EC4}^{*}	Design bending moment considers the second-order effects and member imperfection
N_{ut}	Ultimate load carrying capacity of SCFST column
$N_{FEM,ut}$	Simulated ultimate strength of SCFST column
N_{Ed}	Design value of compressive normal force
$N_{cr,eff}$	Elastic critical load of a composite column corresponding to an effective flexural stiffness
N_{EC4}^{*}	Design value of compressive axial force considers the second-order effects and member imperfection
σ_{rt}	Tensile residual stress
σ_{rc}	Compressive residual stress
σ_{true}	True stress
σ_{true}	True stress
σ_{nom}	Nominal engineering stress
ε_y	Yield strain of steel
ε_{cu}	Ultimate strain of concrete cylinder
ε_{ut}	Axial strain at peak load of SCFST column
ε_{co}	Peak strain of the unconfined concrete
ε_{cc}	Peak strain of the confined concrete
$\varepsilon_{plastic}$	Plastic strain
ε_{nom}	Nominal engineering strain
$\varepsilon_{85\%}$	Axial strain when load drops to 85% of the peak load
ε_{ut}	Axial strain at peak load

Introduction

Concrete-filled steel tubular (CFST) columns are extensively applied in civil engineering infrastructures due to their high compressive strength, stiffness, ductility, good fire resistance capability and excellent energy absorption capacity over reinforced concrete or bare steel section [1–7]. As the steel tube provides formwork for the concrete, no additional shuttering or formwork required for CFST columns, which may not only reduce the cost but also accelerate the speed of construction. Moreover, CFST column reduces the overall section size as well as self-weight of the column which improve the seismic behavior of composite structures. CFST columns with different cross sections including square, rectangular and circular sections are used in various structures,

such as tall buildings, deep foundations, long-span truss bridges, shops, hotel constructions and offshore structures [8, 9]. Among these, square- or rectangular-shaped CFST columns are suitable for building joints and connections because of having higher moment capacities and esthetic aspects. The outer steel section of CFST columns can be fabricated by cold or hot-rolling process. Compared with hot-rolled steel, cold-formed steel sections are widely used in modern buildings owing to their superior execution of strain hardening and fire-resistant property. Moreover, built-up rounded corner hollow steel tubes can be easily manufactured by the utilization of cold-fabrication process. During a severe earthquake, such rounded corner sections could not only delay the plate buckling of steel tubes but also remove the corner cracks of square sections. CFST columns may be subjected to uniaxial or biaxial eccentric compression in several conditions, such as top bearings of the deck girder bridge, corner columns and bottom bearings of the reticular frame. As a result, the behavior and design method of eccentrically loaded CFST columns have become of great interest to many design engineers and research scholars. In recent years, slender CFST columns are being extensively used in high-rise buildings because of providing user-friendly indoor spaces. A column with a global slenderness ratio (L/B) larger than 4 is considered as a slender column [10]. According to the analysis of the test database, about 70% of the total investigation on the eccentrically loaded CFST columns has been reported on low slender and short CFST columns [11]. To date, very few studies have been focused on eccentrically loaded slender CFST columns with various material and geometric properties. Ahmed et al. [12] computationally investigated the buckling behavior of slender square concrete-filled double steel tubular (CFDST) beam-columns under uniaxial eccentric loading and proposed design models for predicting ultimate loads and interaction diagrams of slender CFDST columns. Dong et al. [13] conducted experimental study on rubberized slender CFST columns under uniaxial eccentric compression and concluded that the rubberized concrete infill not only delayed the premature fracture of the outer steel tubes but also improved the ductility and ultimate strength of the specimens. Albero et al. [14] performed experiments to observe the structural performance of eccentrically loaded slender circular CFDST columns. The structural responses of slender concrete-filled narrow rectangular steel tubular (CFNRST) columns under eccentric compression were investigated experimentally by Zhang et al. [15]. Ren et al. [16] inspected the behavior of elliptical slender CFST beam and column under bending and uniaxial eccentric compression. Fu et al. [17] experimentally and numerically investigated the structural behavior of slender rectangular CFST columns with varying wall thickness subjected to eccentric loading. It was reported that the CFST column with varying outer steel tube increased the post-peak

ductility than the column having equal wall thickness under the similar composition. Li et al. [18] investigated the behavior of long square CFST columns having high-strength steel and concrete under eccentric compression. It was observed that the brittle nature of high-strength concrete was talked by high-strength steel tube due to provide higher lateral constraints to the concrete core. More recently, Yuan et al. [19] investigated the structural behavior of built-up stiffened short and slender SCFST columns under eccentric compression. Moreover, Ferhoune [20] studied the influences of crushed slag concrete on the behavior of built-up rectangular low slender CFST columns under eccentric compression. The aforementioned studies are mainly focused on the behavior of eccentrically loaded slender CFST columns, whereas the research on the structural responses of welded built-up slender CFST columns under eccentric compression is still limited. To fill this research gap, the present study reports both experimental and numerical investigations on the structural responses of eccentrically loaded welded built-up slender SCFST columns manufactured with cold-formed rounded corner steel sections. Recently, current design guidelines for conventional CFST columns with standard steel sections are specified in EN 1994-1-1 (European code) [21], AS (Australian code) [22], AISC-360-10 (American code) [23], CSA (Canadian code) [24] and BS 5400 (British standard) [25]. However, the design procedure of eccentrically loaded welded built-up CFST columns is highly conservative due to the shortage of experimental data. Therefore, a series of tests were conducted to study the effects of the concrete strength, column overall slenderness ratio, plate slenderness ratio and variation of eccentricities on failure load and post-peak ductility of the built-up slender SCFST columns under uniaxial eccentric compression. In addition, nonlinear FE models of test columns were developed using ABAQUS software and verified against test results. Finally, the experimental results

(ultimate load and bending moment) were compared with EN 1994-1-1 (EC4) predictions.

Experimental program

Test specimens

In this investigation, a total of eleven slender SCFST columns were tested under uniaxial eccentric compression. Specimens were divided into four groups, where the parameters varied in the tests are as follows: nominal concrete strength ($f_c^/$): 27 to 44 MPa, global or column overall slenderness ratio (*L/B*): 3 to 10, cross-sectional or plate slenderness ratio (*B/t*): 25 to 42 and load eccentricity ratio (*e/B*): 0 to 0.45. The detailed information of the tested columns is presented in Table 1. For convenience, the test specimens were designated according to the shape of the cross section, nominal dimension, concrete cylinder strength and loading eccentricity. For example, the designation S100-4-1000-27-30 defines a square specimen made with cross-sectional dimension of 100 mm × 100 mm where 4 is the wall thickness (*t*) of the outer steel tube in mm, 1000 is the length of the column (*L*) in mm, 27 presents the cylinder strength of infilled concrete ($f_c^/$) in MPa and the last number 30 indicates the applied eccentricity (*e*) in mm.

Material properties

Steel

Prior to column tests, tensile coupon tests were carried out to determine the material properties of the outer steel tubes. Three flat coupon samples were tested for each type of steel tube in accordance with the EN ISO 6892-1 [26],

Table 1 Test data of specimens under uniaxial eccentric compression

Group No	Symbol	Column designation	B x t x L (mm x mm x mm)	B/t	L/B	e/B	$f_c^/$ (MPa)	f_y (MPa)	N_{ut} (kN)	ε_{ut} (µε)	DI	$\delta_{m,ut}$ (mm)	F.M
	E1	S100-4–1000-27–30	100×4×1000	25	10	0.30	27	350	377	6773	2.84	4.80	G+W
1	E2	S100-4–1000-35–30	100×4×1000	25	10	0.30	35	350	466	5884	2.24	2.21	G
	E3	S100-4–1000-44–30	100×4×1000	25	10	0.30	44	350	595	5698	1.48	2.04	G
	E4	S125-5–1000-35–37.5	125×5×1000	25	8	0.30	35	325	693	8821	2.16	2.72	G
2	E5	S125-4–1000-35–37.5	125×4×1000	31	8	0.30	35	350	586	7509	2.11	3.26	G
	E6	S125-3–1000-35–37.5	125×3×1000	42	8	0.30	35	375	482	5928	1.99	4.08	G
	E7	S100-4–300-44–30	100×4×300	25	3	0.30	44	350	801	5908	2.20	1.71	SY
3	E8	S100-4–500-44–30	100×4×500	25	5	0.30	44	350	688	5864	1.80	1.83	SY
	E3	S100-4–1000-44–30	100×4×1000	25	10	0.30	44	350	595	5698	1.48	2.04	G
	E9	S150-5–1000-44–0	150×5×1000	30	7	0	44	325	1474	6928	1.41	3.11	G
4	E10	S150-5–1000-44–45	150×5×1000	30	7	0.30	44	325	968	7796	1.82	3.34	G
	E11	S150-5–1000-44–67.5	150×5×1000	30	7	0.45	44	325	738	11,824	2.11	5.31	G

as detailed in Fig. 1. The measured average elastic modulus, yield stress and ultimate stress of steel specimens are reported in Table 2.

Concrete

Three concrete cylinders with dimensions of 4 inch × 8 inch were cast for each batch (20, 30 and 40 MPa) of concrete mixtures according to the provisions of IS 10262: 2009 [27]. Afterward, axial compression tests were conducted on the concrete cylinders at the same day of CFST column experiment. The average compressive strength of the tested cylindrical specimens has been documented in Table 3

Preparation of specimen

Hollow steel tubes were fabricated from mild steel sheets. At first, the required dimensions were cut from the steel sheet and cold-rolled into half square channel sections. Later, two channels of cold-formed steel were joined through a continuous welding process (Fig. 2). Before concrete casting, a steel plate of 200 mm × 200 mm × 25 mm was welded to the bottom of the tubular steel section. After that, the hollow structural steel tubes were vertically filled with concrete and compaction was done carefully by a poker vibrator. During curing, the top surface of specimens was covered with wet gunny bags for three weeks. After the completion of curing, a small gap was found at the upper portion of each column due to the longitudinal shrinkage of concrete which
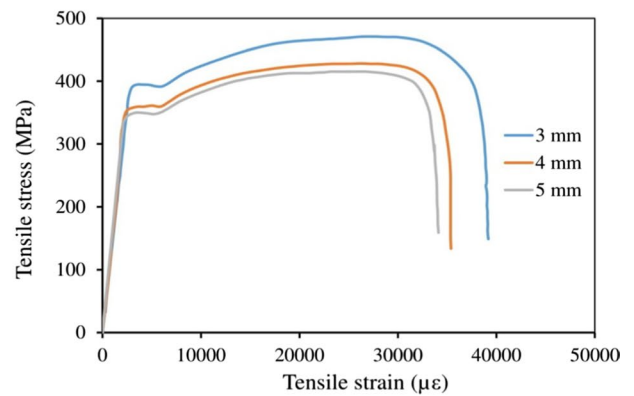
Fig. 1 Details of tensile coupon test
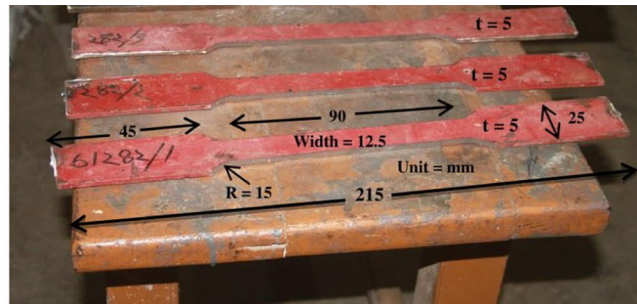
(a) The dimensions of coupon

(b) Tensile testing of specimen   **(c)** Measured tensile stress-strain curves

Table 2 Results of tested tensile coupons

Thickness of steel	Yield stress (f_y)	Elastic modulus (E_s)	Ultimate stress (f_u)	Yield strain (ε_y)	Ultimate strain (ε_{su})
(mm)	(MPa)	(GPa)	(MPa)	($\mu\varepsilon$)	($\mu\varepsilon$)
3	375	215	488	2550	33,159
4	350	200	428	2148	25,167
5	325	196	405	2035	21,213

Table 3 Mixture proportions of plain concrete

Mix design	Cement (OPC)	Water/cement	Coarse aggregate		Fine aggregate	Water	Ave. (f'_c)	Modulus of elasticity (E_c)	Ultimate strain (ε_{cu})	Slump
			¾ inch black stone (70%)	½ inch black stone chips (30%)						
	(Kg/m³)		(Kg/m³)	(Kg/m³)	(Kg/m³)	(Kg/m³)	(Mpa)	(MPa)	(με)	(mm)
M20	355	0.52	711	305	799	185	27	24,734	1900	51
M30	385	0.47	719	308	732.5	181	35	28,160	1750	47
M40	435	0.42	699	299	712	183	44	31,574	1600	39

was filled with high-strength epoxy. Furthermore, grinding was done in order to smooth the top surface of columns. Prior to testing, another steel plate with similar configuration had been welded on the top of those columns for ensuring uniform compression.

Test setup

All columns were tested under axial compression subjected to different load eccentricities. The compressive load was applied by a displacement-controlled 2000 kN Universal Testing Machine (UTM) at a rate of 0.5 mm/min. For ensuring uniaxial eccentric compression and pin–pin boundary condition, both end knife edges were used on the top and bottom position of each specimen, as described in Fig. 3(c). In knife edge setups, outer edge and counterpart inner edge arrangements were adjusted in order to precisely control the load eccentricities. V-shaped outer edge of 50 mm width × 60 mm long was attached to the thick adaptor steel plate at the top and bottom position of the specimens. In the inner edge configuration, V-shaped groove (30 mm depth) was also installed with the base plate (310 mm × 210 mm × 20 mm). The photograph and the schematic view of the test setup are shown in Fig. 3(a) and (b), respectively. Prior to the loading, vertical LVDTs (linear variable differential transducers) having 100 mm length were installed at the end of the columns to determine the axial shortening. Two lateral LVDTs were also attached at 1800 apart to measure the out of plane deflection at the mid-height position of the specimens (Fig. 3(d)). In addition, four axial and lateral strain gauges having the gauge length of 5 mm were installed at 900 apart to determine the longitudinal and transverse strain of the corresponding specimen. Moreover, LabVIEW software was used to collect and analyze the test data. Finally, the unloading operation was done with considering some safety issues: i) axial load dropped to about 65% of the peak load (N_{ut}) ii) more pronounced buckling occurred.

Experimental investigations

Failure modes

During uniaxial eccentric loading, it was observed that the concrete infill, global slenderness ratio (*L/B*) and load eccentricity ratio (*e/B*) had significant influences on the failure modes of the square CFST columns, whereas cross-sectional slenderness ratio (*B/t*) had only moderate effect. The buckling modes obtained from the experiments are shown in Fig. 4. Close observation of the tested columns leads to the following:

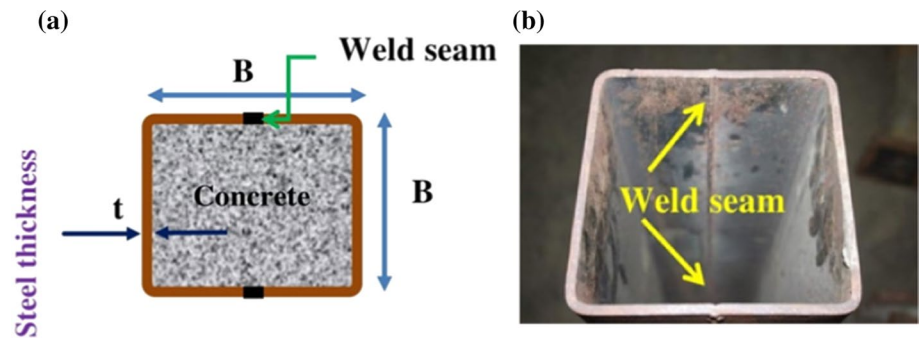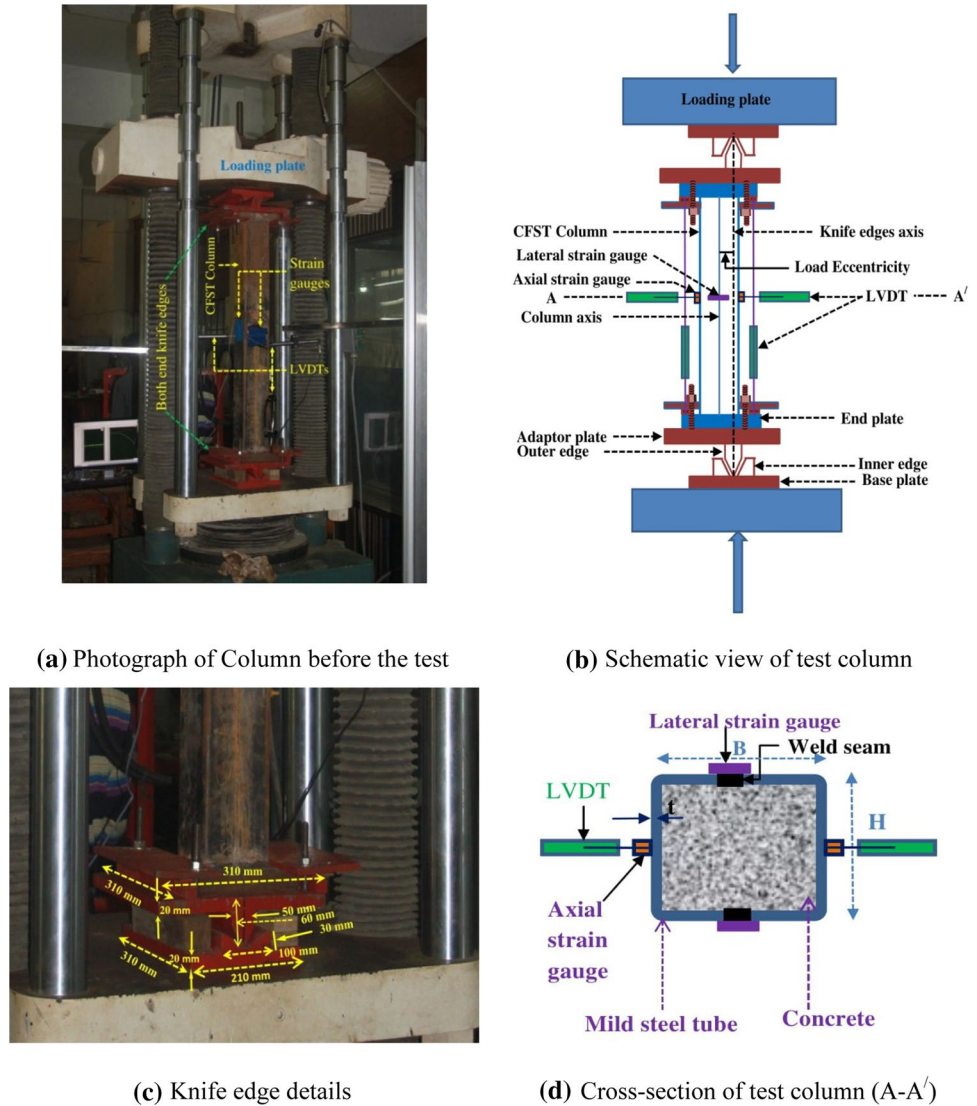**Fig. 2** Cold-formed welded steel tubular section

Fig. 3 Test setup

(**a**) Photograph of Column before the test

(**b**) Schematic view of test column

(**c**) Knife edge details

(**d**) Cross-section of test column (A-A$^/$)

(i) Generally, the eccentrically loaded columns exhibited a moderate lateral deflection due to the generation of secondary moment. For columns (E1, E2 and E3) with higher slenderness ratio ($L/B = 10$), failure was observed to occur by global buckling, as exhibited in Fig. 4(a). This is probably owing to the fact that columns with higher L/B ratio had larger flexibility resulting in greater mid-height lateral deformation. Similar failure behavior was observed for columns E4, E5 and E6 where the value of L/B ratio was 8 (Fig. 4(b)). It is worth mentioning that buckling of the specimen was initially observed after the yielding of steel in the compression zone, which was accompanied by the cracking of concrete
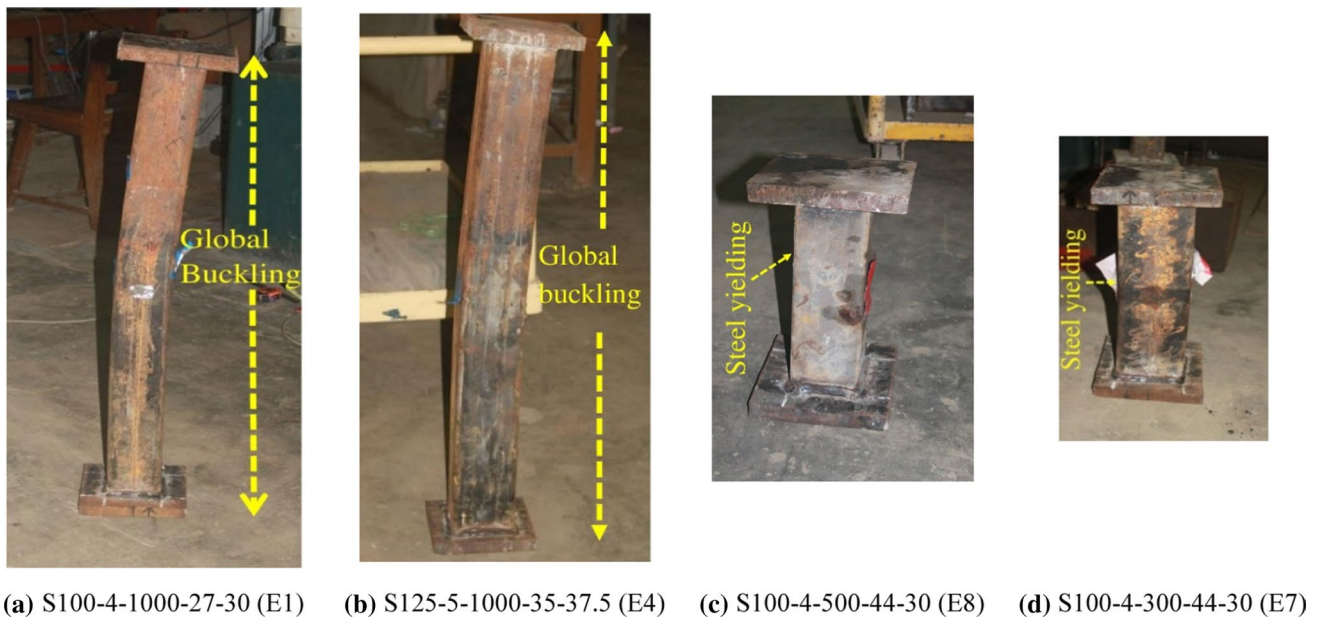
(a) S100-4-1000-27-30 (E1) **(b)** S125-5-1000-35-37.5 (E4) **(c)** S100-4-500-44-30 (E8) **(d)** S100-4-300-44-30 (E7)

Fig. 4 Failure modes of test specimens

in the tension zone. Along with the global bucking, welding failure was observed in column E1 due to generation of more tensile stresses in the welding region. Moreover, no pronounced outward local buckling was noticed around the specimens' cross section at failure because of small *B/t* ratios (25–42) of the tested columns. Due to the use of rounded corner section, cracks were not observed at the corners of the specimens. This clearly indicates that the round corner section exhibits better structural performance under eccentric axial compression.

(ii) Failure was initiated by steel yielding which was followed by the cracking of concrete in stockier columns (E7 and E8) with lower *L/B* ratio (*L/B* = 5 and 3), as presented in Fig. 4 (c and d). This can be explained by the fact that columns with lower L/B ratio showed greater rigidity and compactness which resulted in smaller mid-height lateral deflection.

0(iii) Columns E9, E10 and E11 (L/B ratio = 7) subjected to different e/B ratio (0, 0.30 and 0.45) showed overall flexural buckling due to the generation of excess second-order moment.

Axial load versus axial strain curves

The axial load (*N*) versus axial strain (*ε*) curves of the tested columns are displayed in Fig. 5, where both solid circles and dotted lines represent the observed buckling and yield strain from steel coupon test, respectively. In Fig. 5, the axial loads were obtained from the readings of universal testing machine (UTM) and the axial strains were computed from both strain gauges and LVTD's.

Before tube buckling, the strain gauges were used to determine the axial strain. After that, the axial displacement readings of LVDT's were divided by overall length (Δ/L) of the test specimens to obtain the strain. It is noticed that the *N*-*ε* curves exhibited similar behavior for all square slender CFST columns subjected to eccentric loading. A typical *N*-*ε* curve can be divided into five stages, i.e., an elastic stage, an elastic–plastic stage until the peak load is achieved, a descending stage which represents the decrease of the confinement between steel tube and concrete core due to the propagation of micro-cracks in core concrete as well as outward buckling of the steel tube, respectively, and a stable stage which is followed by an unloading stage. As can be observed from Fig. 5(a) that the initial stiffness and ultimate load (N_{ut}) significantly increased with the increase of concrete strength (f_c'). This is because of the formation of lesser micro-cracks in higher strength concrete. Such kind of formation may occur due to the smooth nature of the fracture surface which situates between the interfacial transition zone and aggregate in higher strength concrete [28]. However, columns with lower strength concrete experienced earlier buckling than that of the CFST columns infilled with higher strength concrete. This behavior may be interpreted by the fact that lower strength concrete dilates much quicker than higher strength concrete. It is also observed that specimens filled with higher strength concrete suddenly dropped the peak load after reaching the ultimate strength owing to the brittle nature of higher strength concrete. Meanwhile, columns with lower *B/t* ratio noticeably exhibited higher initial rigidity and buckling load compared to specimens with higher *B/t* ratio, as

(a) Effect of concrete strength

(b) Effect of *B/t* ratio

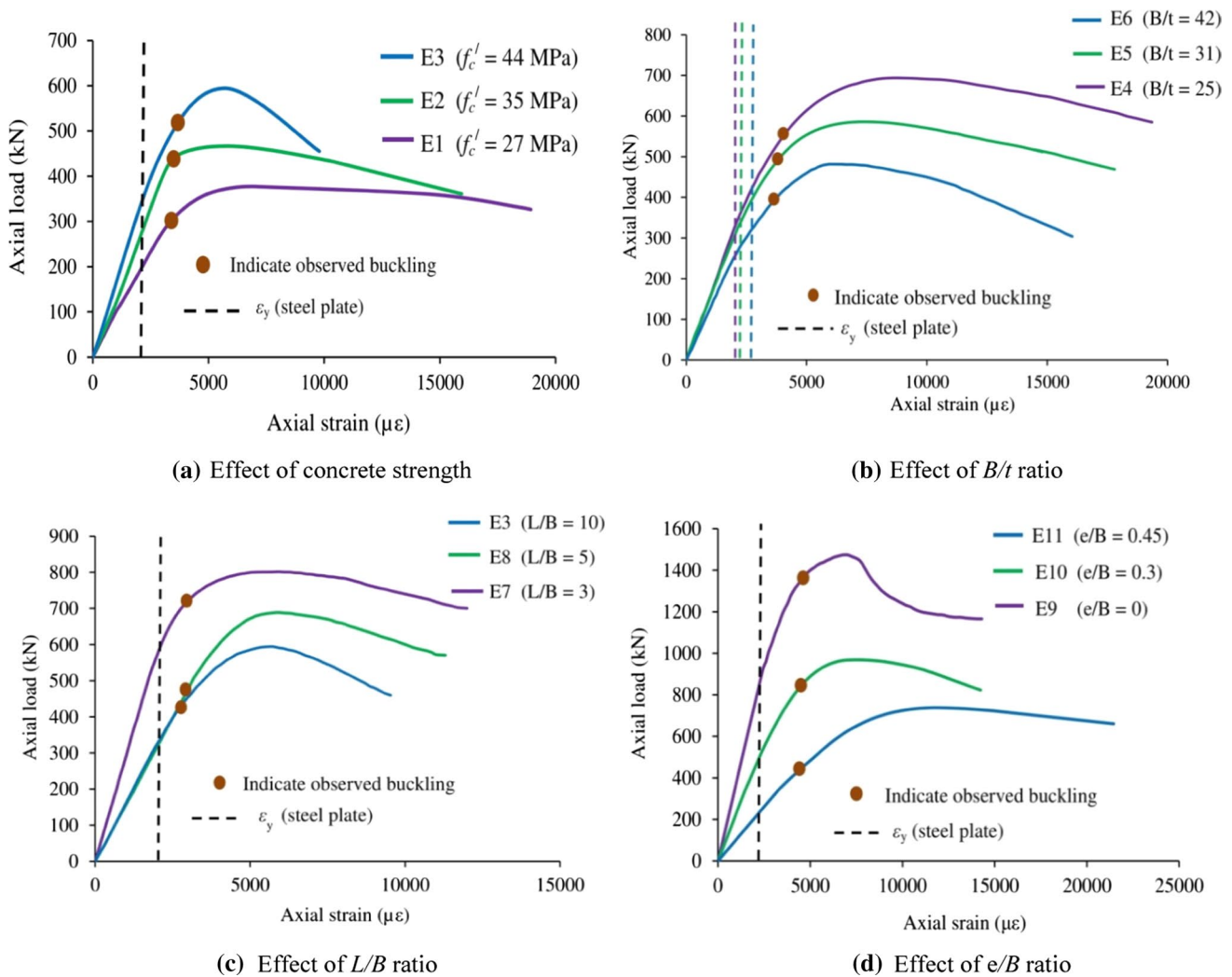**(c)** Effect of *L/B* ratio

(d) Effect of e/*B* ratio

**Fig. 5** Effects of different parameters on axial load versus axial strain curves

presented in Fig. 5(b). This is due to the fact that thicker steel tube could provide extra support or confinement to the core concrete resulting in better composite interaction. Moreover, the ascending slope and peak load of tested columns conspicuously decreased with the increase of overall slenderness ratio (*L/B*) (Fig. 5(c)). This is because the columns having higher *L/B* ratio showed larger flexibility which resulted instability during the application of eccentric compression. In the softening stage, the descending branch showed a steeper slope for columns with greater *L/B* ratio. It can be deduced that the confinement effect between outer steel tube and concrete core decreased with the increase of *L/B* ratio. As expected the ascending slope and cross-sectional capacity decreased with the increase of load-eccentricity ratio (e/B) because of uneven transformation of load through the cross section of the specimens (Fig. 5(d)). It is also observed that, specimens with larger

e/B ratio experienced earlier buckling since the load is quickly transferred to the adjacent steel tube wall.

Ultimate axial strength

Ultimate axial strength has been defined as the maximum cross-sectional strength of the tested columns under the applied loading conditions. The measured ultimate strengths are presented in Table 1 and plotted in Fig. 6 against f_c', B/t, L/B and e/B ratio. As can be noticed from Fig. 6(a), the ultimate axial strength (N_{ut}) of specimens was found to improve by 24% and 58% when the concrete compressive strength (f_c') increased from 27 to 35 MPa and 44 MPa, respectively. This can be explained by the fact that high-strength concrete possesses better internal bond and larger elastic modulus which improves the ultimate strength of composite columns. On the other hand, it is noticed that the N_{ut} of the tested

Fig. 6 Effects of different parameters on ultimate strength of test specimens
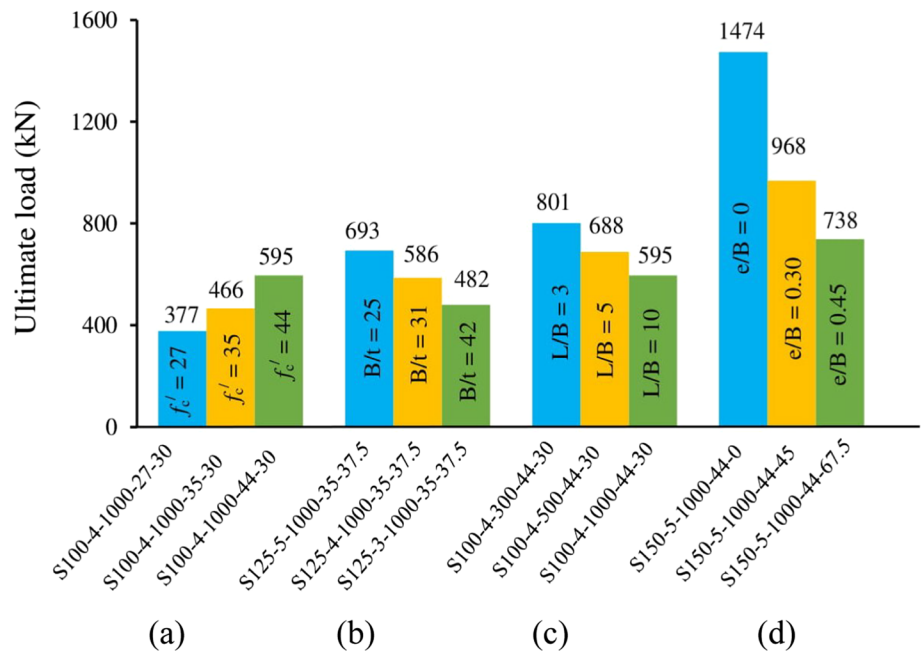
columns decreased by 16% and 31% with the increase of *B/t* ratio from 25 to 31 and 42, respectively (Fig. 6(b)). This may be attributed to the lower rigidity and load-carrying capability of the specimens with thinner steel tube than that of thicker counterpart. Moreover, Fig. 6(c) illustrates that with the increase of *L/B* ratio moderately decreased the ultimate capacity of the tested specimens. This is owing to the fact that the materials of specimens with higher *L/B* ratio had not been fully utilized. Besides, it can also be observed from Fig. 6(d) that N_{ut} remarkably decreased by 35% and 50% when *e/B* ratio increased from 0 to 0.30 and 0.45, respectively. As expected, when load eccentricity is applied, the

ultimate load decreases rapidly due to the generation of excess second-order moment.

Ductility Index

In this study, ductility index is adopted to evaluate the ductility of test specimens. Ductility index has been defined as the ratio of the axial strain ($\varepsilon_{85\%}$) when load drops to 85% of the peak load (N_{ut}) in the descending stage and corresponding strain (ε_{ut}) at N_{ut} [29], as described in Fig. 7.

Hence,

Fig. 7 Effects of different parameters on ductility index of test specimens
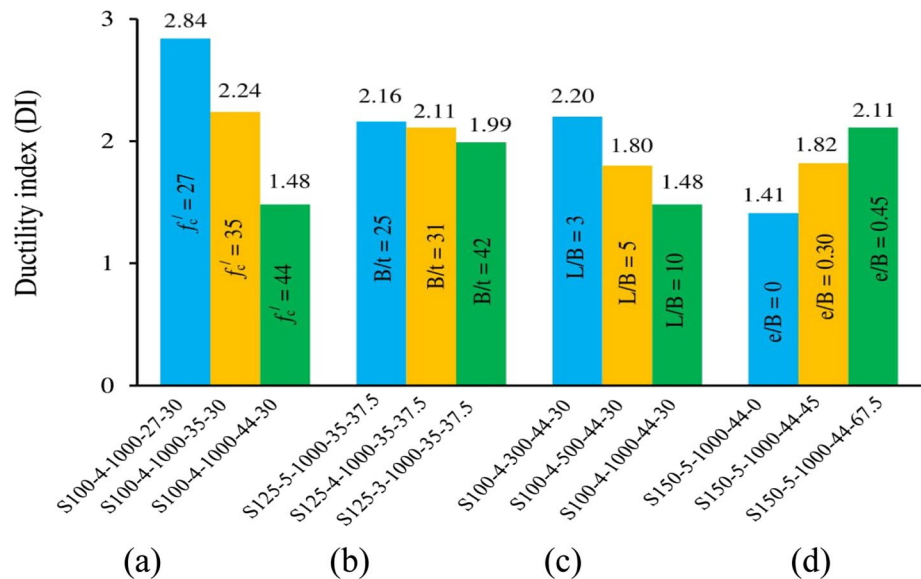
$$DI = \frac{\varepsilon_{85\%}}{\varepsilon_{ut}} \tag{1}$$

It would appear from Fig. 7(a) that with the increase of the concrete strength causes a significant reduction of DI. As previously discussed, the brittle nature of higher strength concrete is responsible for this fact. However, the DI slightly decreased with the increase of *B/t* ratio (Fig. 7(b)), since thinner steel tube provides less confinement to the concrete core. Moreover, specimens with higher *L/B* ratio showed lower DI, as shown in Fig. 7(c). This can be explained by the fact that the confinement between the steel tube and concrete core decreases with the increase of the overall slenderness ratio (*L/B*). In addition, it is quite interesting to observe from Fig. 7(d) that the DI increased by 29% and 49% when the load eccentricity ratio increased from 0 to 0.30 and 0.45, respectively. In fact, this is not surprising since non-directly loaded concrete and adjacent steel tube could provide extra support to the partially loaded concrete in specimens with higher *e/B* ratio, as described in Fig. 8.

Mid-height deflection

Generally, eccentrically loaded columns exhibit moderate lateral deflection due to the generation of second-order moment. Initially, when the applied load was small, no remarkable increase of the lateral deflection of the specimens was observed. When the applied load reached about 60% to 70% of the peak load (N_{ut}), the columns started flexing and the mid-height deflection increased significantly. During the tests, two transverse strain gauges and two LVDTs at mid-height were used to measure the lateral deflection. In order to compute the mid-height deflection: the average values of transverse strain gauges were used before buckling of steel
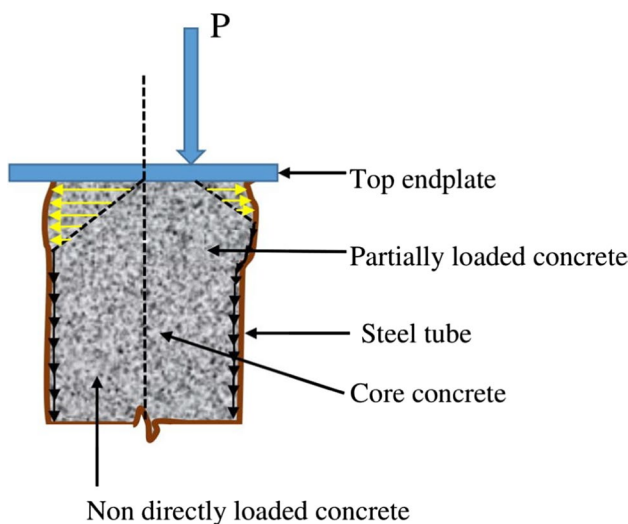

Fig. 8 Mechanism of load transformation

tube and afterward, displacement readings of the LVDTs were taken. As can be observed from Fig. 9(a) that the mid-height deflection at peak load ($\delta_{m,ut}$) of CFST columns significantly decreased with the increase of f_c'. This is owing to the fact that the higher strength concrete dilates much slower than normal strength concrete. However, similar results were not achieved by thinner steel tubes. Figure 9(b) depicts that $\delta_{m,ut}$ remarkably increased by 20% and 46% when *B/t* ratio increased from 25 to 31 and 42, respectively. This implies that sufficient restriction to the lateral deformation of concrete could not be achieved by thinner steel tubes than that of thicker counterparts. Meanwhile, Fig. 9(c) exhibits similar tendencies according to the previous figure, when the *L/B* ratio increased, the $\delta_{m,ut}$ also increased. This is because of the specimens with higher slenderness ratio (*L/B*), buckle much quicker before achieving its full strength. Moreover, from Fig. 9(d), it is worth mentioning that with the increase of *e/B* ratio noticeably increased the $\delta_{m,ut}$ of the tested columns. As discussed earlier, this is owing to the generation of excess second-order moment of specimens having higher *e/B* ratio.

Finite element analysis

Model description

In this study, the ABAQUS software [30] was employed to develop the FE models of eccentrically loaded built-up slender SCFST columns. The description and verification of the FE models are summarized below. It is noted that welding residual stresses and geometric imperfections were considered in the full-column model. The eight-noded linear brick elements (C3D8R), having three translational degrees of freedom at each node were utilized in the meshing of both outer steel tube and concrete infill. After the mesh sensitivity studies, an average element size of 20 mm was applied for achieving accurate results with reasonable time. From tensile coupon tests, the obtained engineering stress–strain curves were translated into true stress and plastic strain curves for inputting into ABAQUS. The true stress (σ_{true}), true strain (ε_{true}) and plastic strain ($\varepsilon_{plastic}$) can be calculated from the following expression.

$$\sigma_{true} = \sigma_{nom}(1 + \varepsilon_{nom}) \tag{2}$$

$$\varepsilon_{true} = In(1 + \varepsilon_{nom}) \tag{3}$$

$$\varepsilon_{plastic} = \varepsilon_{true} - (\sigma_{true}/E_s), \tag{4}$$

where σ_{nom} and ε_{nom} represent the nominal engineering stress and strain, respectively.

(a) Core concrete strength

(b) Plate slenderness ratio

(c) Global slenderness ratio
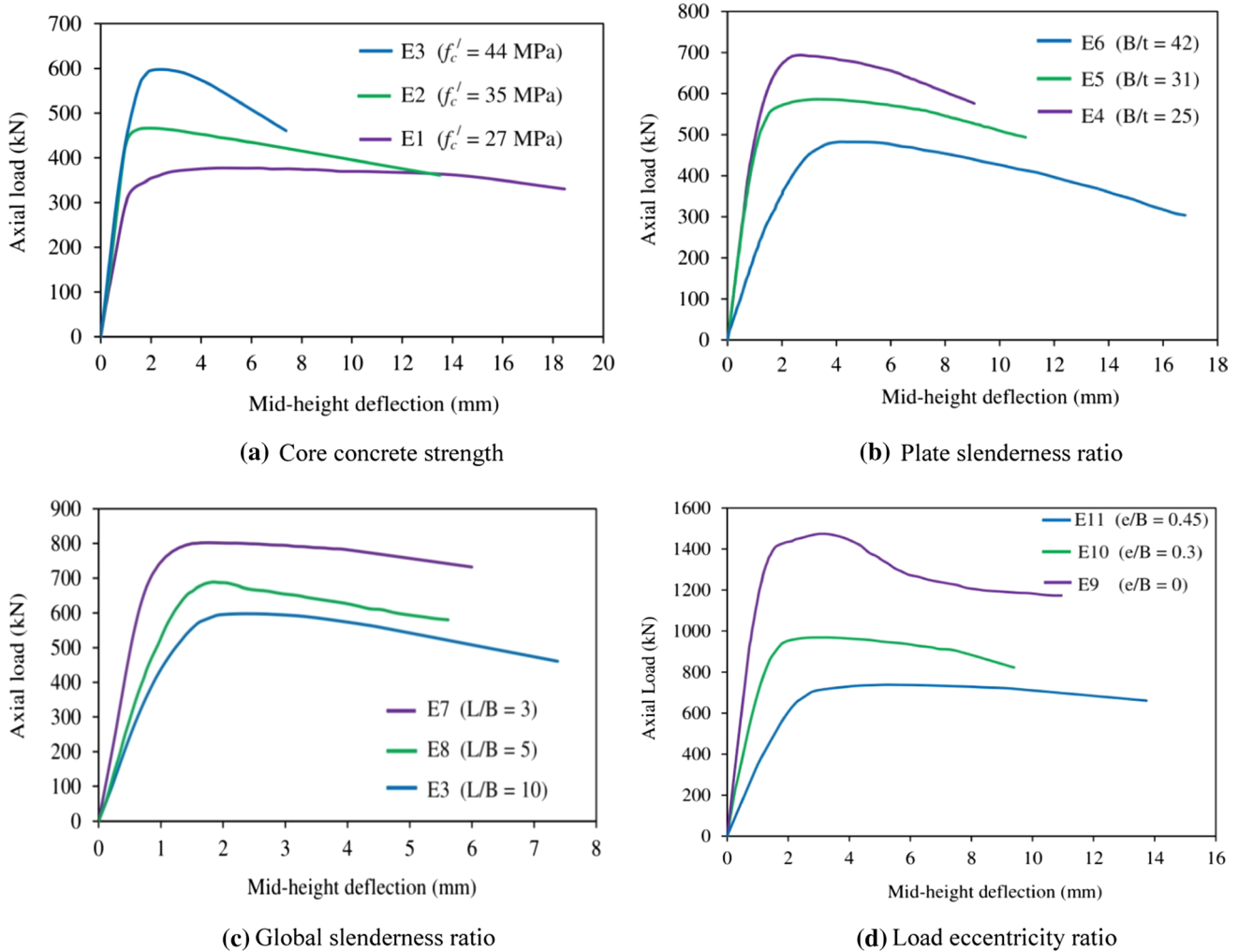
(d) Load eccentricity ratio

Fig. 9 Effects of different parameters on mid-height deflection of test specimens

The concrete damaged plasticity (CDP) model available in ABAQUS was adopted to consider the plasticity behavior of concrete, where the plasticity parameters, such as dilation angle (ψ), viscosity parameter (μ) and flow potential eccentricity (e) were taken as 40^0, 0 and 0.1, respectively, as suggested by Tao et al. [31] In order to characterize the compressive behavior of confined concrete, a three-stage model proposed by Tao et al. [31] was adopted in this paper (Fig. 10), which is expressed as follows,

$$\sigma = \begin{cases} \left[\dfrac{A\cdot(\varepsilon/\varepsilon_{c0})+B\cdot(\varepsilon/\varepsilon_{c0})^2}{1+(A-2)\cdot(\varepsilon/\varepsilon_{c0})+(B+1)\cdot(\varepsilon/\varepsilon_{c0})^2}\right]\cdot f_c', & 0 < \varepsilon \leq \varepsilon_{c0} \\ f_c', & \varepsilon_{c0} < \varepsilon \leq \varepsilon_{cc} \\ f_r + (f_c' - f_r)\exp\left[-\left(\dfrac{\varepsilon-\varepsilon_{cc}}{\alpha}\right)^{\beta}\right], & \varepsilon_{cc} < \varepsilon \end{cases} \quad (5)$$

, where ε_{c0} and ε_{cc} represent the peak strain of the unconfined and confined concrete, respectively; A, B, α and β are material parameters; f_r is the residual stress of concrete.
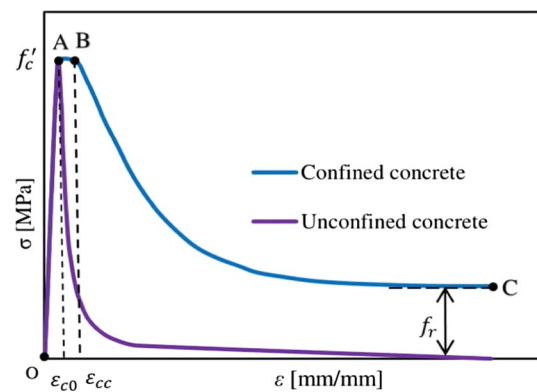

Fig. 10 Proposed stress–strain model for confined concrete [31]

Meanwhile, tensile softening response of concrete was considered to be linear up to 10% of the concrete cylinder strength. The inelastic part of the concrete under tension was considered by stress-crack opening displacement

relationship, which was characterized by means of the fracture energy (G_F) [32] (given in Eq. 5).

$$G_F = (0.0469d_{max}^2 - 0.5d_{max} + 26)(\frac{f_c^{/}}{10})^{0.7}, \qquad (6)$$

where d_{max} is the maximum size of coarse aggregate (20 mm).

The surface to surface contact algorithm was considered to model the interfaces between the steel tube and the concrete infill. The outer circumference of the concrete infill was selected as the master surfaces, while the inner surface of the steel tube was defied as the slave surfaces. Along the normal direction, a 'hard contact' was applied, where no penetration was allowed between two interfaces. On the other hand, coulomb friction model having a coefficient of 0.3 was defined along the tangential direction. Geometric imperfections are commonly noticed after the fabrication of CFST members, which have significant influence on the buckling shapes of the steel tubes under compression [33]. After the sensitivity studies, the magnitude of the global imperfection was chosen as $L/1000$, where L is the total length of the specimen. At first, an eigenvalue buckling analysis was performed for each column to acquire the appropriate imperfection pattern. The shape of the geometric imperfections was included in the nonlinear FE models with the lowest buckling mode obtained from the eigenvalue analysis. Moreover, residual

Fig. 11 Residual stress distribution in outer steel tube

Fig. 12 Typical finite element model with load and boundary condition

stresses generated due to welding, were considered in the FE models. According to the experimental observations, the maximum tensile residual stress (σ_{rt}) takes place near the weld centerline and its magnitude is almost the yield strength of the steel (f_y). On the other hand, the magnitude of the compressive residual stress (σ_{rc}) was taken as $0.2 f_y$ [34]. Typical residual stress distribution in the steel tube is displayed in Fig. 11. The top and bottom surfaces of each CFST columns were coupled with two reference points, where the desired load eccentricity was applied by a displacement-controlled mode. For top RP (reference point), all degrees of freedom were fixed except for the rotation about x-x axis ($U1 = U2 = 0$, $UR2 = UR3 = 0$) and the vertical displacement along z-direction. However, only rotation about x-x axis was allowed for bottom reference point. In this analysis, the static RIKS procedure was adopted. A typical FE model of the built-up slender SCFST column is presented in Fig. 12.

Model verification

The accuracy of the models is evaluated by comparing the test and numerical results in terms of the failure modes, axial load versus axial strain curves and ultimate strengths. Figure 13 represents the comparison of buckling modes obtained from the test and FE analysis. It can be clearly noticed from Fig. 13 that the predicted failure modes are very similar to the observed failure modes. In addition, the simulated load versus axial strain curves (N_{FEA}-ε) and the corresponding load versus mid-height deformation (N_{FEA}-δ_m) curves of the specimens were also compared against the test results, as exhibited in Fig. 14 and 15, respectively. Due to page restriction, only test curves of two specimens are presented herein. Figure 14 indicates that both ascending and descending parts of the predicted load versus deformation curves almost coincide with corresponding experimental curves. Moreover, good agreement was observed between the simulated ultimate strength ($N_{FEM,ut}$) and measured N_{ut} from test results, where the mean value
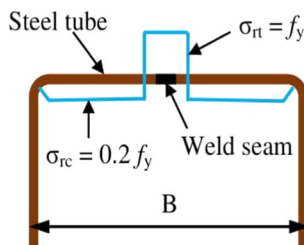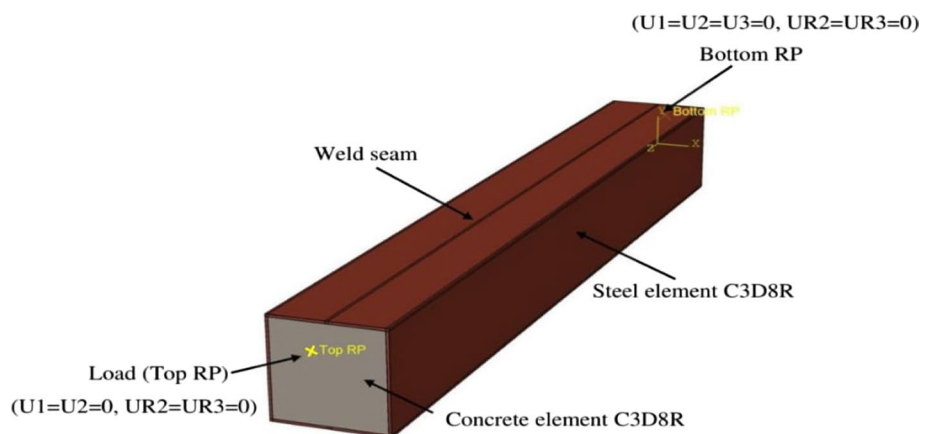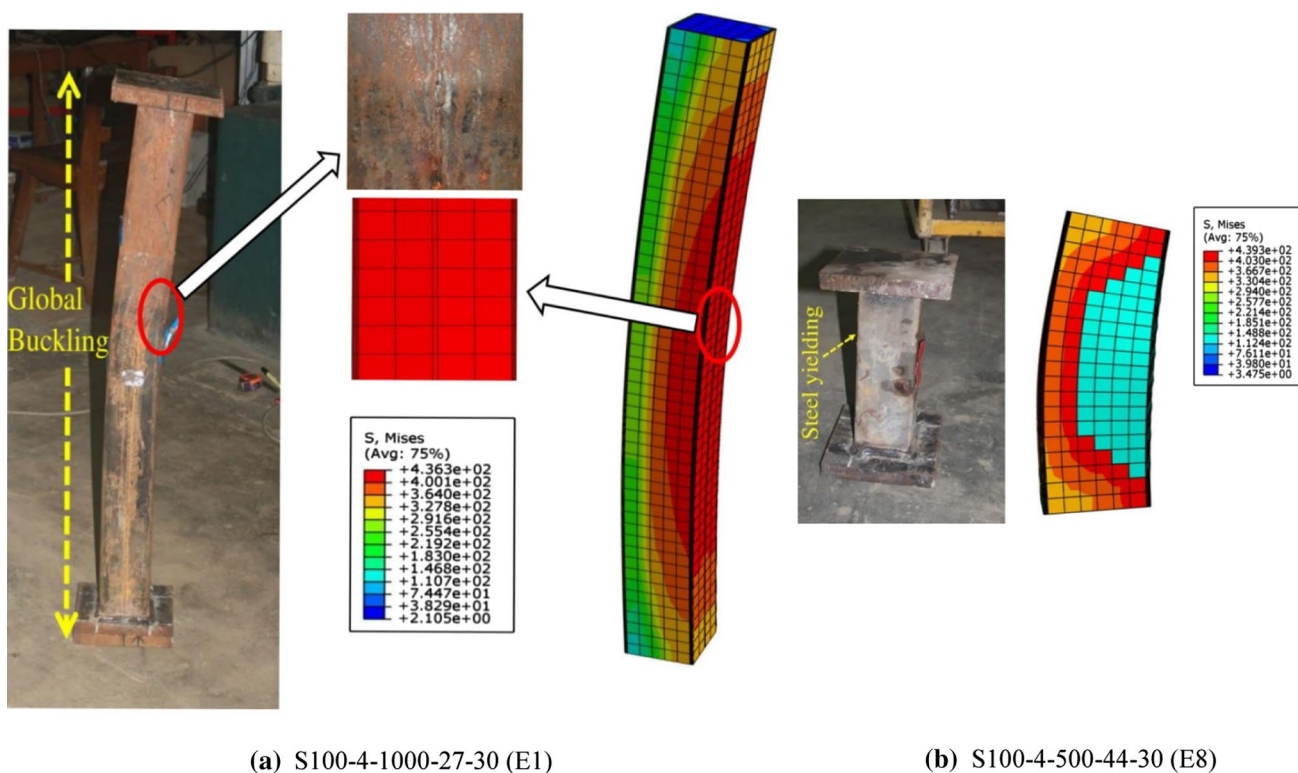
(a) S100-4-1000-27-30 (E1)　　　　　　　　　　　　　　**(b)** S100-4-500-44-30 (E8)

Fig. 13 Comparison of buckling modes obtained from experiment and FE simulation

(a) S100-4-1000-27-30 (E1)　　　　　　　　　　　　　　**(b)** S100-4-500-44-30 (E8)
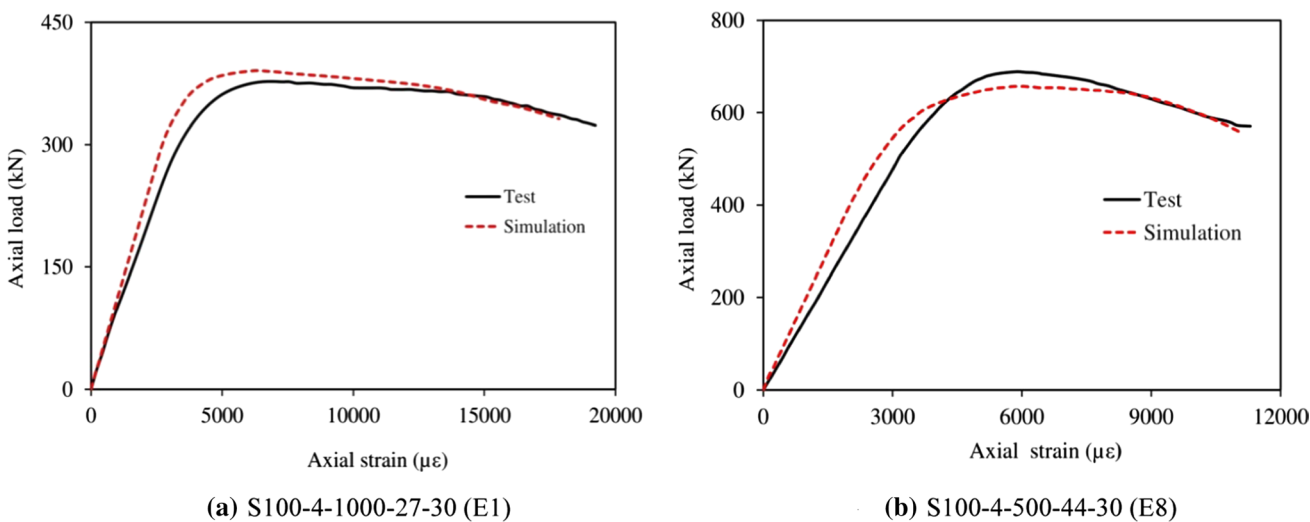
Fig. 14 Comparison of experimental and predicted axial load-axial strain curves

of $N_{FEM,ut}/N_{ut}$ is equal to 1.020 with the corresponding standard deviation (SD) of 0.084 (Table 4). Therefore, it can be concluded that the developed models are capable of accurately predicting the structural behavior of SCFST columns.

Comparison of test results with EN 1994-1-1 predictions
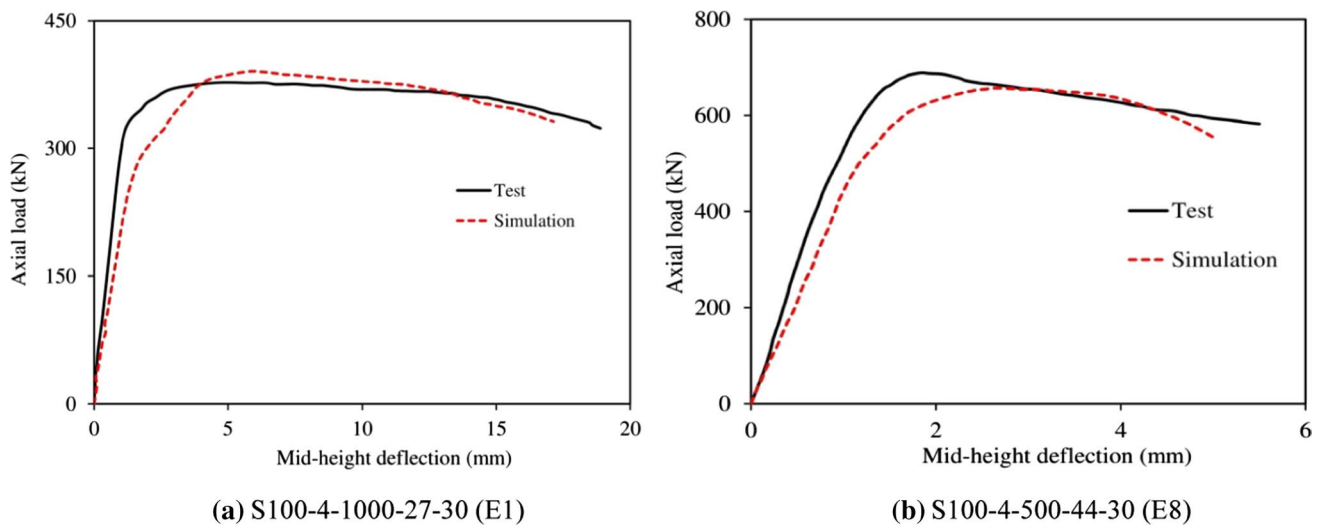
In this investigation, the applicability of EN 1994-1-1

Fig. 15 Comparison of experimental and predicted axial load-mid-height deflection curves

Table 4 Comparison of experimental and FEA strengths for SCFST columns

Specimen	N_{ut} (kN)	$N_{FEM,ut}$ (kN)	$N_{FEM,ut}/N_{ut}$
S100-4-1000-27-30	377	390	1.03
S100-4-1000-35-30	466	463	0.99
S100-4-1000-44-30	595	526	0.88
S125-5-1000-35-37.5	693	740	1.07
S125-4-1000-35-37.5	586	676	1.15
S125-3-1000-35-37.5	482	578	1.20
S100-4-300-44-30	801	683	0.85
S100-4-500-44-30	688	654	0.95
S150-5-1000-44-0	1474	1580	1.05
S150-5-1000-44-45	968	1060	1.09
S150-5-1000-44-67.5	738	765	1.03
Mean			1.020
SD			0.084

specifications [21] is assessed to predict the ultimate axial strength and maximum flexural moment of built-up slender SCFST columns. The European standard (EC4) which is based on structural steel design, allows both strain-compatibility method and plastic stress distribution method. Note that the ultimate bending moments of the eccentrically loaded columns were computed from $M_{ut} = N_{ut}$ $(e + \delta_{m,ut})$, where $\delta_{m,ut}$ is the second-order mid-height displacement at peak load and e is the load eccentricity. According to the clause 6.7.3.6 (1), from the EN 1994-1-1 which provides the following expression for combined compression and uniaxial bending:

$$\frac{M_{Ed}}{M_{pl,N,Rd}} \leq \alpha_M, \tag{7}$$

where M_{Ed} represents the design bending moment which considers both second-order moment and column imperfection within the column overall length; and $M_{pl,N,Rd}$ is the design value of plastic bending moment which counts the compressive axial force N_{Ed}. In this study, the value of the coefficient α_M is taken as 0.9 for columns with f_y up to 375 MPa [14].

The second-order effects is considered by multiplying the first-order design bending moment by an amplification factor k which can be obtained from Eq. (8):

$$k = \frac{\beta}{1 - \frac{N_{Ed}}{N_{cr,eff}}}, \tag{8}$$

where β is an equivalent moment factor included in Table 4 from EN 1994-1-1 and $N_{cr,eff}$ represents the elastic critical axial force which considers the column overall length corresponding to the effective flexural stiffness. Moreover, According to Table.5 from EN 1994-1-1, a member imperfection of $L/300$ is considered for rectangular square hollow steel section where the value of the amplification factor k is taken as 1.0. In this study, all reduction factors and material safety factors has been taken as unity. As can be noticed from Table 5, EC4 overestimated the ultimate strength of the eccentrically loaded columns by about 6% on average and gave an unsafe prediction. This can be interpreted by the fact that EC4 takes into account the full confining effect for square shaped CFST columns. At the time of considering second-order effects and member imperfection, EC4[*] provided slightly unsafe prediction of ultimate loads of the specimens with mean and SD of 1.01 and 0.11, respectively.

Table 5 Comparison of EN 1994-1-1 predictions with experimental results

Symbol	Column designation (mm x mm x mm)	N_{ut} (kN)	N_{EC4} (kN)	N_{EC4}^{*} (kN)	M_{ut} (kN-m)	M_{EC4} (kN-m)	M_{EC4}^{*} (kN-m)	N_{EC4}/N_{ut}	N_{EC4}^{*}/N_{ut}	M_{EC4}/M_{ut}	M_{EC4}^{*}/M_{ut}
E1	S100-4-1000-27-30	377	406	391	13.11	13.19	12.33	1.07	1.03	1.01	0.95
E2	S100-4-1000-35-30	466	470	446	15.00	14.50	13.25	1.01	0.95	0.97	0.90
E3	S100-4-1000-44-30	595	530	500	19.06	16.00	15.22	0.90	0.85	0.84	0.81
E4	S125-5-1000-35-37.5	693	791	767	27.90	29.35	28.25	1.14	1.10	1.05	1.02
E5	S125-4-1000-35-37.5	586	710	692	23.88	26.87	25.92	1.21	1.18	1.13	1.08
E6	S125-3-1000-35-37.5	482	631	610	20.04	23.71	20.21	1.30	1.26	1.16	0.99
E7	S100-4-300-44-30	801	530	500	25.43	16.00	15.22	0.66	0.63	0.63	0.60
E8	S100-4-500-44-30	688	530	500	21.92	16.00	15.22	0.78	0.73	0.73	0.70
E9	S150-5-1000-44-0	1474	1859	1859	0	0	0	1.26	1.26	0	0
E10	S150-5-1000-44-45	968	1078	1015	46.83	48.54	45.78	1.11	1.04	1.03	0.98
E11	S150-5-1000-44-67.5	738	888	812	53.73	59.83	56.23	1.20	1.10	1.11	1.04
Mean								1.06	1.01	0.88	0.82
Standard deviation								0.10	0.11	0.16	0.19

M_{EC4}^{*} considers the second-order effects and member imperfection ($\alpha_M = 0.90$)

M_{EC4} does not consider the second-order effects and member imperfection

Besides, both cases are conservative for predicting the ultimate bending moment. Therefore, these comparisons clearly indicate that EC4* provisions are more accurate to be used for eccentrically loaded slender built-up SCFST columns. The comparisons between experimental results and EC4 predictions are shown in Fig. 16.

The axial load (N) versus bending moment (M) curves of the tested columns are presented in Fig. 17, where solid blue line represents the 0.9 M–N interaction diagram including second-order effects and imperfection. In addition, black point at intersection between the α_M M–N interaction diagram (solid blue line) and the bending moment curve (dotted black line) indicates the predicted failure load (N_{EC4}^{*}) and bending moment (M_{EC4}^{*}), respectively. As can be observed from Fig. 17(a, b and c) that, EC4 provides much safer predictions for the specimens with higher concrete compressive strength. Meanwhile, non-conservative prediction of EC4 increased with the increasing of both B/t and L/B ratio, respectively. It is crucial here to note that EC4 remained unsafe for the prediction of the specimens with higher load eccentricity ratio (e/B), as observed in Fig. 17(i).

Conclusions

In this study, a total of eleven built-up slender SCFST columns were tested under uniaxial eccentric compression having various geometric and material properties. The effects of different parameters including the concrete strength, column overall slenderness ratio, plate
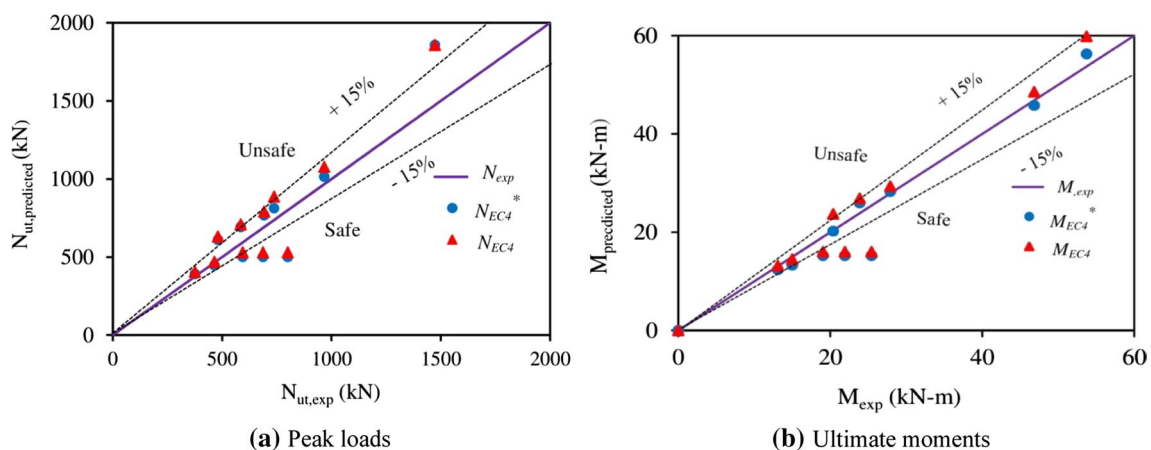

(a) Peak loads　　　　　　　　**(b)** Ultimate moments

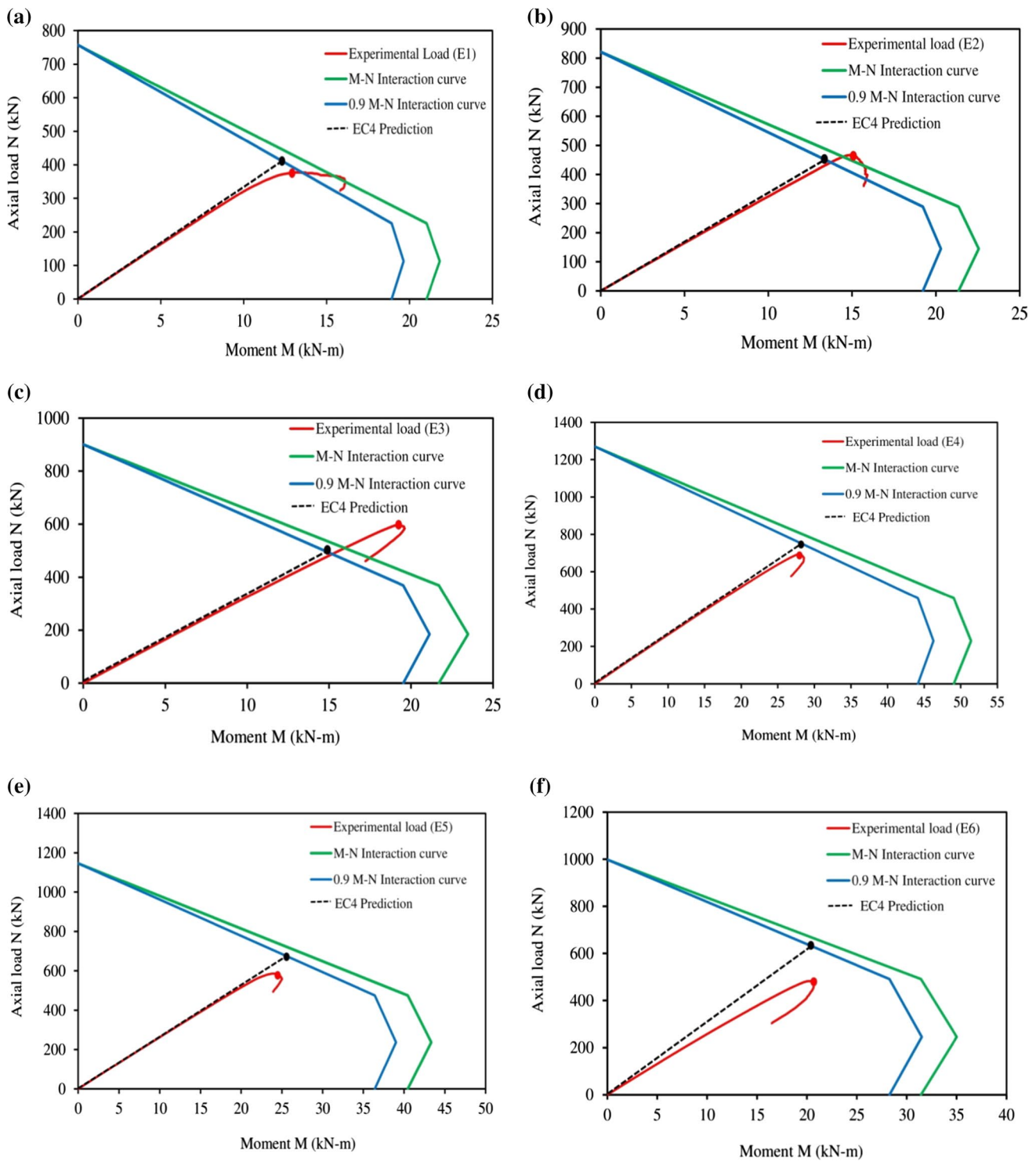**Fig. 16** Comparisons between experimental results and EC4 predictions

Fig. 17 Axial load (*N*) versus Moment (*M*) interaction curves of composite columns (a) E1 ($f_c^l = 27$), (b) E2 ($f_c^l = 35$), (c) E3 ($f_c^l = 44$), (d) E4 (*B/t* = 25), (e) E5 (*B/t* = 31), (f) E6 (*B/t* = 42), (g) E7 (*L/B* = 3), (h) E8 (*L/B* = 5), (i) E9,E10, E11 (*e/B* = 0, 0.30, 0.45)

slenderness ratio and variation of eccentricities on the buckling modes, ultimate axial strength and post-peak ductility of the specimens were investigated. Furthermore, nonlinear FE models of tested specimens were developed and verified against experimental results. Finally, the experimental results (ultimate load and bending moment) were compared with EN 1994-1-1 provisions for eccentrically loaded columns. Based on the experimental results,
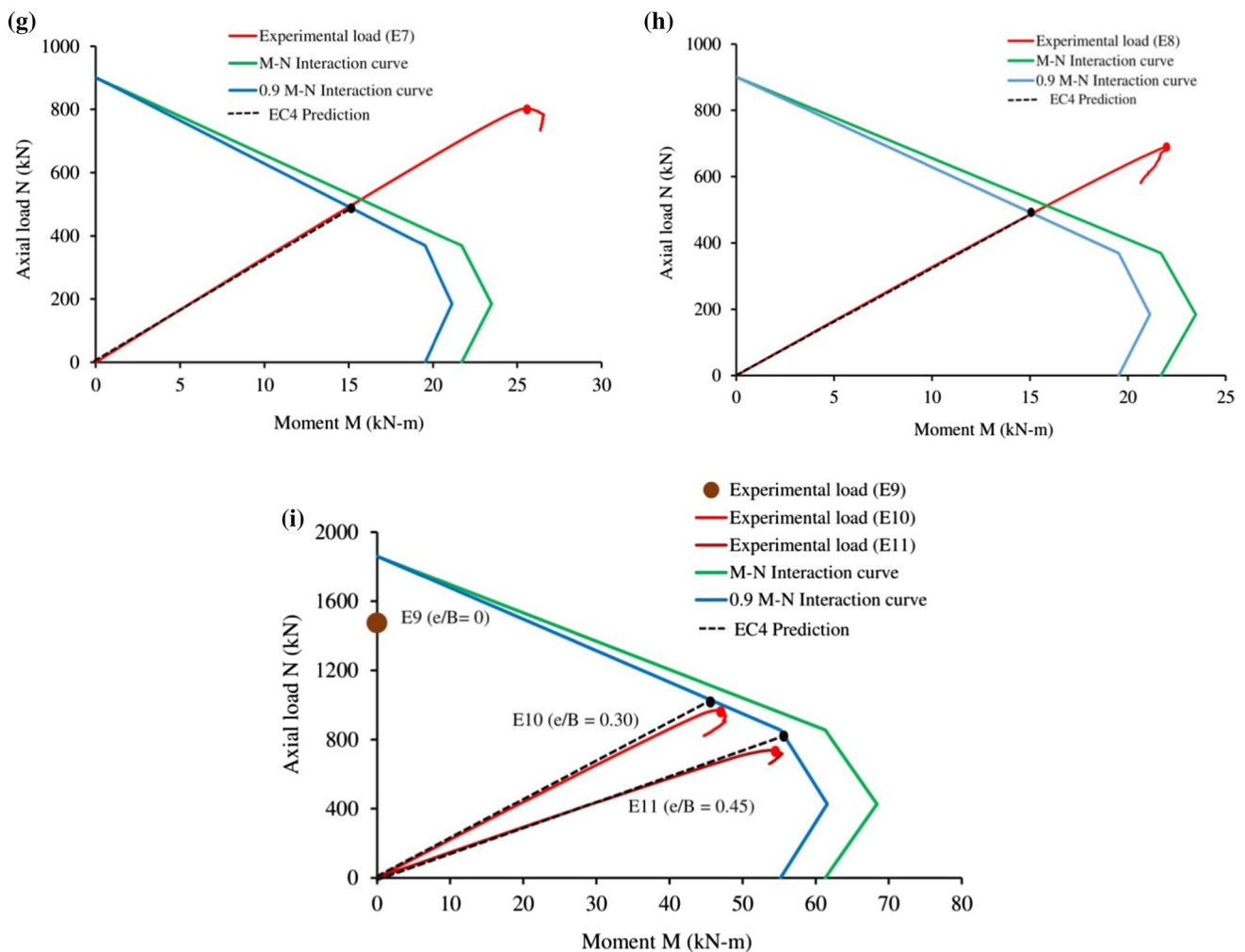
Fig. 17 (continued)

the following conclusions can be reached within the scope of the current studies.

(1) The typical failure mode of the eccentrically loaded columns with higher slenderness ratio ($L/B = 7$ and 10) was characterized by global buckling, where the buckling was initiated by steel yielding which was followed by cracking of concrete at the tension side of the corresponding specimens. In addition, cracking of concrete and steel yielding also occurred in stockier columns with lower L/B ratio ($L/B = 3$ and 5).

(2) The behavior of tested specimens is greatly influenced by the global slenderness ratio (L/B), plate slenderness ratio (B/t) and the variation of eccentricity under compression. The initial stiffness and ultimate axial strength of columns decreased with the increase of overall slenderness or eccentricity. Moreover, the ultimate strength as well as ductility of the tested specimens moderately decreased with the increase of plate slenderness ratio.

(3) Mid-height deflection at peak load ($\delta_{m,ut}$) of the eccentrically loaded CFST columns significantly decreased with the increase of concrete strength, while it increased with the increase of B/t ratio, L/B ratio and e/B ratio, respectively.

(4) EN 1994-1-1 slightly overestimated the ultimate axial strength by 1% when second-order effects and column imperfection were considered.

(5) The developed FE models are capable of accurately predicting the structural behavior of SCFST columns. The validated models can be used for further parametric studies to predict the ultimate loads and interaction diagrams of built-up slender CFST columns under combined compression and bending.

Declaration

Conflict of interest On behalf of all authors, the corresponding author declares that they have no competing interests.

References

1. Han L, Li W, Bjorhovde R (2014) Developments and advanced applications of concrete-filled steel tubular (CFST) structures: Members. J Constr Steel Res 100:211–228. https://doi.org/10.1016/j.jcsr.2014.04.016

2. Oliveira De W, Nardin De S, Cresce El De Debs A, Debs M El (2009) Influence of concrete strength and length/diameter on the axial capacity of CFT columns. J Constr Steel R. 65:2103–2110. https://doi.org/10.1016/j.jcsr.2009.07.004

3. Abramski M (2018) Load-carrying capacity of axially loaded concrete-filled steel tubular columns made of thin tubes. Arch Civil Mechan Eng 18:902–913. https://doi.org/10.1016/j.acme.2018.01.002

4. Chan T, Huai Y, Wang W (2015) Experimental investigation on lightweight concrete-filled cold-formed elliptical hollow section stub columns. J Constr Steel Res 115:434–444. https://doi.org/10.1016/j.jcsr.2015.08.029

5. Tao Z, Han L, Wang D (2008) Strength and ductility of stiffened thin-walled hollow steel structural stub columns filled with concrete. Thin-Walled Struct 46:1113–1128. https://doi.org/10.1016/j.tws.2008.01.007

6. EkmekyaparAL-Eliwi TB (2016) Experimental behaviour of circular concrete filled steel tube columns and design specifications. Thin-Walled Struct 105:220–230. https://doi.org/10.1016/j.tws.2016.04.004

7. Liew J, Xiong M, Xiong D (2016) Design of Concrete Filled Tubular Beam-columns with High Strength Steel and Concrete. Structures 8:213–226. https://doi.org/10.1016/j.istruc.2016.05.005

8. Vrcelj Z, Uy B (2002) Strength of slender concrete-filled steel box columns incorporating local buckling. J Constr Steel Res 58:275–300. https://doi.org/10.1016/s0143-974x(01)00045-1

9. Chen C, Ko J, Huang G, Chang Y (2012) Local buckling and concrete confinement of concrete-filled box columns under axial load. J Constr Steel Res 78:8–21. https://doi.org/10.1016/j.jcsr.2012.06.006

10. Tao Z, Brian U, Han L, He S (2008) Design of concrete-filled steel tubular members according to the australian standard as 5100 model and calibration. Aust J Struct Eng 8:197–214. https://doi.org/10.1080/13287982.2008.11464998

11. Thai S, Thai H, Uy B, Ngo T (2019) Concrete-filled steel tubular columns: Test database, design and calibration. J Constr Steel Res 157:161–181. https://doi.org/10.1016/j.jcsr.2019.02.024

12. Ahmed M, Liang Q, Patel V, Hadi M (2019) Local-global interaction buckling of square high strength concrete-filled double steel tubular slender beam-columns. Thin-Walled Struct 143:106244. https://doi.org/10.1016/j.tws.2019.106244

13. Dong M, Elchalakani M, Karrech A, Hassanein M, Xie T, Yang B (2019) Behaviour and design of rubberised concrete filled steel tubes under combined loading conditions. Thin-Walled Struct 139:24–38. https://doi.org/10.1016/j.tws.2019.02.031

14. Albero V, Ibañez C, Piquer A, Hernández-Figueirido D (2021) Behaviour of slender concrete-filled dual steel tubular columns subjected to eccentric loads. J Constr Steel Res 176:106365. https://doi.org/10.1016/j.jcsr.2020.106365

15. Zhang L, Mao C, Xiao-Gang L, Tong G, Jing T, Wang Y (2020) Experimental study on CFNRST members under combined compression and bending. J Constr Steel Res 167:105950. https://doi.org/10.1016/j.jcsr.2020.105950

16. Ren Q, Han L, Lam D, Li W (2014) Tests on elliptical concrete filled steel tubular (CFST) beams and columns. J Constr Steel Res 99:149–160. https://doi.org/10.1016/j.jcsr.2014.03.010

17. Fu G, Fu G, Yu C, Li S, Wang F, Yang J (2021) Behaviour of rectangular concrete-filled steel tubular slender column with unequal wall thickness. Eng Struct 236:112100. https://doi.org/10.1016/j.engstruct.2021.112100

18. Li G, Chen B, Yang Z, Liu Y, Feng Y (2021) Experimental and numerical behavior of eccentrically loaded square concrete-filled steel tubular long columns made of high-strength steel and concrete. Thin-Walled Struct 159:107289. https://doi.org/10.1016/j.tws.2020.107289

19. Yuan F, Huang H, Chen M (2019) Effect of stiffeners on the eccentric compression behaviour of square concrete-filled steel tubular columns. Thin-Walled Struct 135:196–209. https://doi.org/10.1016/j.tws.2018.11.015

20. Ferhoune N (2014) Experimental behaviour of cold-formed steel welded tube filled with concrete made of crushed crystallized slag subjected to eccentric load. Thin-Walled Struct 80:159–166. https://doi.org/10.1016/j.tws.2014.02.014

21. EN 1994–1–1: Design of Composite Steel and Concrete Structures (2004). Eurocode 4, Brussels, Belgium

22. AS5100: Bridge Design-steel and Composite Construction (2004). Australian Standard, Australia

23. AISC-360–10: Specification for Structural Steel Buildings (2010). American Institute of Steel Construction, Chicago, USA

24. CSA Standard S16: Design of steel structures (2009). Canadian Standards Association, Ontario. Canada

25. Steel, Concrete and Composite Bridges, Part 5, (BS.5400–5) (2002): code of practice for design of composite Bridges

26. EN ISO 6892–1. Metallic Materials – Tensile Testing – Part 1: Method Of Test At Room Temperature (2009). European Committee for Standardization (CEN), Brussels

27. IS: 10262–1982, recommended guidelines for concrete mix design, Bureau of Indian Standards, New Delhi, India

28. Taerwe L (1991) Brittleness versus ductility of high strength concrete. Struct Eng Int 1(4):40–45. https://doi.org/10.2749/101686691780617166

29. Han L, Ren Q, Li W (2011) Tests on stub stainless steel–concrete–carbon steel double-skin tubular (DST) columns. J Constr Steel Res 67:437–452. https://doi.org/10.1016/j.jcsr.2010.09.010

30. ABAQUS analysis user's manual (2018) Version 6:14

31. Tao Z, Wang Z, Yu Q (2013) Finite element modelling of concrete-filled steel stub columns under axial compression. J Constr Steel Res 89:121–131. https://doi.org/10.1016/j.jcsr.2013.07.001

32. Bažant Z, Becq-Giraudon E (2002) Statistical prediction of fracture parameters of concrete and implications for choice of testing standard. Cem Concr Res 32:529–556. https://doi.org/10.1016/s0008-8846(01)00723-2

33. Tao Z, Uy B, Han L, Wang Z (2009) Analysis and design of concrete-filled stiffened thin-walled steel tubular columns under axial compression. Thin-Walled Struct 47:1544–1556. https://doi.org/10.1016/j.tws.2009.05.006

34. Uy B (1998) Concrete-filled fabricated steel box columns for multistorey buildings: behaviour and design. Prog Struct Mat Eng 1:150–158. https://doi.org/10.1002/pse.2260010207